Atmospheric
Chemistry
and Physics

Stratospheric ozone interannual variability (1995–2011) as observed by lidar and satellite at Mauna Loa Observatory, HI and Table Mountain Facility, CA

G. Kirgis, T. Leblanc, I. S. McDermid, and T. D. Walsh

Jet Propulsion Laboratory, California Institute of Technology, Table Mountain Facility, Wrightwood, California, USA

Correspondence to: G. Kirgis (kirgis@tmf.jpl.nasa.gov)

Abstract. The Jet Propulsion Laboratory (JPL) lidars, at the Mauna Loa Observatory, Hawaii (MLO, 19.5° N, 155.6° W) and the JPL Table Mountain Facility (TMF, California, 34.5° N, 117.7° W), have been measuring vertical profiles of stratospheric ozone routinely since the early 1990's and late-1980s respectively. Interannual variability of ozone above these two sites was investigated using a multi-linear regression analysis on the deseasonalised monthly mean lidar and satellite time-series at 1 km intervals between 20 and 45 km from January 1995 to April 2011, a period of low volcanic aerosol loading. Explanatory variables representing the 11 yr solar cycle, the El Niño Southern Oscillation, the Quasi-Biennial Oscillation, the Eliassen-Palm flux, and horizontal and vertical transport were used. A new proxy, the mid-latitude Ozone Depleting Gas Index, which shows a decrease with time as an outcome of the Montreal Protocol, was introduced and compared to the more commonly used linear trend method. The analysis also compares the lidar time-series and a merged time-series obtained from the space-borne Stratospheric Aerosol and Gas Experiment II, Halogen Occultation Experiment, and Aura-Microwave Limb Sounder instruments.

The results from both lidar and satellite measurements are consistent with recent model simulations which propose changes in tropical upwelling. Additionally, at TMF the Ozone Depleting Gas Index explains as much variance as the Quasi-Biennial Oscillation in the upper stratosphere. Over the past 17 yr a diminishing downward trend in ozone was observed before 2000 and a net increase, and sign of ozone recovery, is observed after 2005. Our results which include dynamical proxies suggest possible coupling between hori-zontal transport and the 11 yr solar cycle response, although a dataset spanning a period longer than one solar cycle is needed to confirm this result.

1 Introduction

The concentration and distribution of stratospheric ozone is determined by three processes: in situ creation (production), in situ destruction (loss), and transport into or out of the region. In the upper stratosphere (35–45 km) the first two processes, ozone production and loss, are primarily homogeneous photochemical processes taking place mostly where the effects of Ozone Depleting Substances (ODSs) are expected to be the easiest to quantify (UNEP/WMO Ozone Assessments, 1999). Below about 30 km, the lifetime of ozone is comparable to, or longer than, transport time scales and ozone is strongly affected by transport.

Detecting recent trends in ozone variations has been central to understanding if the Montreal Protocol is working. Studies referenced in WMO (2010) pointed out that ozone levels, both in total column and vertical distribution, were stabilising. They concurred that the first stage of recovery (i.e., slowing of ozone decline attributable to ODSs changes) had already occurred and that the second stage (i.e., onset of ozone increase) was expected to become evident within the next two decades. Recent studies confirm that the upper stratospheric ozone decline apparent from 1979 until the mid-1990s has stopped, stabilising around 1995–1996, and has a statistically insignificant trend after 1998 (Jones et al., 2009; Steinbrecht et al., 2009; Tatarov et al., 2009).

In the tropical lower stratosphere (LS, 20–25 km), the work of Randel and Thompson (2011) exhibits statistically significant negative trends (approximately −2 to −4 % per decade). Such an ozone trend is simulated in many current chemistry-climate models as a result of a systematic increase in tropical stratospheric upwelling (Eyring et al., 2010; Shepherd, 2008; Li et al., 2009; Waugh et al., 2009).

Most ozone is found in the lower stratosphere and therefore column ozone measurements largely reflect the distribution in the lower stratosphere. These observations exhibit significant asymmetry between the hemispheres, with the differences maximising in the winter–spring seasons (McConnell and Jin, 2008). Dynamics explains this asymmetry as well as why ozone loss exhibits high year-to-year variability while the halogen loading responsible for its chemical loss evolves more smoothly. Dynamical variability leads to changes in ozone abundance through changes in transport. It follows that in order to detect and attribute the chemical ozone loss resulting from anthropogenic halogens, it is necessary to understand and account for the role of dynamics (Shepherd, 2008). Quantifying ozone variability and trends from historical observations is a clue to understand past changes and contribute to validating models used to predict future evolution of global ozone (Randel and Thompson, 2011).

Adding to these historical observations are the two JPL differential absorption lidars located at Table Mountain Facility, California, and Mauna Loa Observatory, Hawaii, which have been routinely measuring stratospheric ozone profiles since the late 1980s and the early 1990s, respectively. The lidars vertical sampling resolution is 300 m, and the effective resolution of the ozone profiles range from less than 1 km in the lower stratosphere to 4 km in the upper stratosphere. Under the framework of the Network for Detection of Stratospheric Composition Change (NDACC, formerly NDSC), these ground-based routine measurements support the validation of satellite measurements (Leblanc et al., 2006), and produce long-term monitoring reference datasets (Leblanc and McDermid, 2000; Li et al., 2008). They constitute unique and invaluable datasets to study the long-term ozone variability in the subtropical and mid-latitude regions.

Other historical observations (going back at least two decades) are the space-borne Stratospheric Aerosol and Gas Experiment II (ERBS-SAGE-II), Halogen Occultation Experiment (UARS-HALOE), and Microwave Limb Sounder (Aura-MLS). These satellite instruments provide high-quality observations to compare with our ground-based lidars over both sites. SAGE II and HALOE datasets span from 1995 to 2005 and the Aura-MLS dataset (hereafter referred to as MLS for brevity) complements the time series since 2004. Usually, zonal averaging of datasets is applied over large latitude bands before using a multi-linear regression analysis (Soukharev and Hood, 2006; Remsberg, 2008). However, recently Randel and Thompson (2011), combining Southern Hemisphere Additional Ozonesonde (SHADOZ) and SAGE II over single tropical sites from 1984 to 2009,

found statistically significant negative trends in the tropical lower stratosphere (approximately −2 to −4 % per decade over ∼ 17–21 km).

Multi-linear statistical models using explanatory variables (or proxies) are commonly used to extract interannual and long-term ozone variability (see ref. in WMO, 2011, chapter 2; Randel and Thompson, 2011). The influence of the Quasi-Biennial Oscillation (QBO), the 11 yr solar cycle (SC_{11}) and the El Niño Southern Oscillation (ENSO) on both total column ozone and vertical distribution have all been identified, but as discussed in WMO (2007), a sizable fraction of the interannual or long-term ozone changes can also be related to other dynamical processes. The estimation of trends requires a proper accounting for the effect of these processes on ozone. One approach is to add more terms to the model used for trend calculations using statistics and letting the regression model find the best proxies (e.g., Mäder et al., 2007). Another way is to add proxies based on possible physical processes that cause the ozone changes (e.g., Wohltmann et al., 2007). The two studies using these approaches (Mäder et al., 2007; Wohltmann et al., 2007) introduced a new proxy to isolate horizontal advection and vertical transport (Wohltmann et al., 2005) and showed that the introduction of this proxy in the statistical model led to the removal of most other dynamical variables (Mäder et al., 2007). In this paper, we used a multi-linear regression analysis on deseasonalised monthly mean lidar and satellite time-series with explanatory variables representing the 11 yr solar cycle, the El Niño Southern Oscillation, the Quasi-Biennial Oscillation, and horizontal and vertical transport. We also added the vertical component of the Eliassen-Palm flux (EPf) across the mid-latitude tropopause to express a measure of the divergence of the momentum flux that drags the residual circulation and determines large-scale ozone transport (see also, Reinsel et al., 2005; Dhomse et al., 2006; Jrrar et al., 2006, Jain, 2010).

In the next section, the JPL lidar and satellite datasets used are described and their use for long-term analysis discussed. Our regression model and its different components are detailed in Sect. 3. Results for each proxy are presented and discussed in Sect. 4.

2 Lidar and satellite data sets

The JPL lidar group has a long record of lidar measurements. Three Differential Absorption Lidars (DIAL) have been operated for the long-term monitoring of ozone and temperature in the troposphere and stratosphere at Mauna Loa Observatory, Hawaii (MLO, 19.5° N, 155.6° W) and the JPL Table Mountain Facility, California (TMF, 34.4° N, 117.7° W). The two stratospheric systems utilise Rayleigh and vibrational Raman scattering. Two laser beams (308 nm and 353 nm) are emitted in the atmosphere. The backscattered light is collected by a telescope and sent to two receiving channels at

308 nm, two at 353 nm, one at 332 nm, and one at 385 nm. The signals are used to retrieve stratospheric ozone number density between 15 and 55 km (Leblanc and McDermid, 2000). Ozone mixing ratio is then derived using air density and temperature obtained from lidar or from daily NCEP analysis. At MLO almost 100 % of the mixing ratio profiles were derived using temperature measured by lidar, while at TMF only 50 % were derived this way. The lidar measurements yield high vertical resolution for all altitudes below 35 km and are typically integrated over two nighttime hours beginning at the end of astronomical twilight. At both sites, only one significant change in instrumental configuration occurred (in 2000 at MLO and 2001 at TMF) and results are produced with the same family of analysis programs (i.e., only minor changes in processing versions), this ensures highly consistent datasets over 2.5 decades. Nonetheless, no measurements of the TMF lidar are available around the year 2000. A close look at the daily profiles for each DIAL pair of channels, as well as at the altitudes where these pairs were combined to form a unique profile (15–50 km) confirmed that there was no "jump" in the time-series associated with the instrumentation or data processing. Though the Raman channels (15–35 km range) provide measurements almost insensitive to aerosols, we selected our time window from 1995 to 2011 to avoid periods of heavy volcanic aerosol loading. For each site this ensures that the dataset is internally consistent and suitable for trends and interannual variability studies. The best quality measurements (typical relative uncertainty less than 3 %) cover the 20–40 km altitude range. The relative uncertainty comprises measurement and retrieval. It includes the statistical uncertainty associated with the measurement (precision), and the combined uncertainty associated with the lidar signal saturation correction and atmospheric extinction correction. From January 1995 to April 2011, more than 2000 lidar profiles were measured at MLO and more than 1100 at TMF.

SAGE II, onboard the Earth Radiation Budget Satellite (ERBS), provided two decades of ozone observations from 1984 to 2005. SAGE II version 6 retrieval algorithms have ∼ 1 km or less vertical resolution and the precision of the ozone observation is usually better than 1 % in the middle stratosphere increasing to 2 % near the stratopause and tropopause (Manney et al., 2001). Number density profiles from version 6.2 were used and converted to mixing ratio versus altitude using the air density profile provided with these data.

Ozone mixing ratio profiles from HALOE onboard UARS are measured by the attenuation of the Sun's intensity in a broadband channel centered at 9.6 μm. Version 19 ozone profiles vertical range is from 15 to 60 km and the instrument vertical resolution is close to 2 km. Error estimates vary from 5 to 10 % in the middle and upper atmosphere (Bhatt et al., 1999).

EOS/Aura was launched in 2004. Onboard Aura, the Microwave Limb Sounder (MLS) instrument measures ther-

mal emissions from the limb of Earth's atmosphere. The latitudinal data coverage from 82° S to 82° N. Compared to version 2.2, ozone is now reported on the "high resolution" grid: spaced at 12 surfaces per decade (∼ 1.3 km).and transition back to the regular 6-surfaces-per-decade grid at 1.0 hPa (∼ 2.5 km spacing). As recommended by Froidevaux et al. (2008), ozone profiles used are in the 215 to 0.02 hPa with status, precision and quality values that give total errors of from 5 to 10 %. Interpolation of the ozone mixing ratio profiles onto an altitude grid was made using geopotential height profiles available in version 3.3.

The need for a consistent dataset to be used for the study of stratospheric ozone recovery led us to the construction of a homogenized time-series from the three instruments introduced above. In order to be compared with the lidar time series, a merged satellite dataset was formed for each station by using ozone mixing ratio collocated profiles (±5° latitude, ±25° longitude). To build the merged satellite time series from 1995 to 2005, the average of HALOE and SAGE II measurements was used. The best agreement with the lidar time series was to interpolate each satellite measurements on a 2 km vertical grid. Then, the averaged differences between the merged HALOE+SAGE II values and the MLS values over the overlapping period June 2004–May 2005 were used to correct the MLS measurements from 2005 to 2011. For both lidar and merged-satellite datasets, ozone mixing ratio monthly means were calculated and deseasonalised by subtracting the climatological mean for each month from January 1995 to April 2011. Due to the low number of HALOE and SAGE II coincidences, it was found that relaxing time coincidences and thus using every profile available in a month over each site leads to lower biases between merged-satellite and lidar time series and better correlation coefficients (usually up to 18–19 %) between the regression model results.

The left side of Fig. 1 shows the number of profiles used to calculate the monthly means for each station (MLO on top and TMF below). At MLO, for the lidar and the satellite merged time-series, the mean number of profiles used for each month is 11.2 for the lidar, 4.3 for SAGE II, 5.5 for HALOE and 29.7 for MLS. At TMF, in the same order, the average numbers are 7.7, 6.7, 5.9 and 29.7. If only time coincidences were used, these numbers would be at MLO: 1.1 for SAGE II, 0.3 for HALOE and 8.9 for MLS and 1.4 for SAGE II, 0.3 for HALOE and 5.2 for MLS at TMF. Due to the occultation measurements method, HALOE and SAGE II yield fewer coincidences. Average probabilities to have a coincidence with a lidar measurement from the three satellite measurements are at MLO (respectively TMF) 10 % (25 %) for SAGE II, 3 % (7 %) for HALOE and 89 % (91 %) for MLS. For each time series, data gaps were filled by interpolation, only if at least two measurements on each side of the missing value could be used. The right side of Fig. 1 shows a comparison between the lidar (in red) and the merged satellite (in black) deseasonalised time series. The
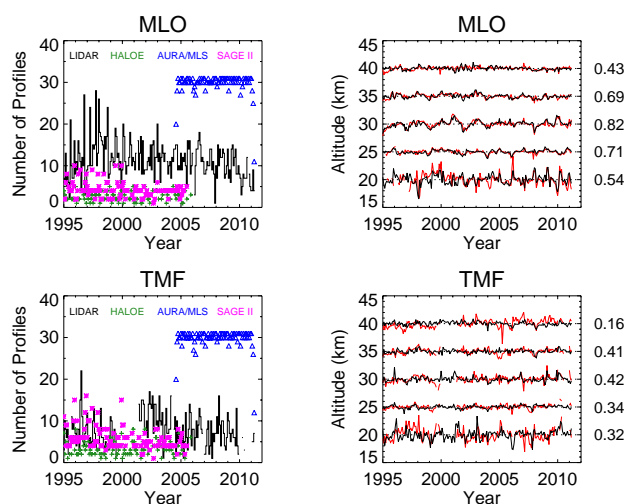
Fig. 1. Left: number of profiles by month for MLO (top) and TMF (bottom) from 1995 to 2012. Right: ozone anomalies time series (lidar in red, merged satellite time series in black) for MLO (top) and TMF (bottom). The ozone perturbation scale is $10\,\%\,\mathrm{km}^{-1}$. The numbers on the right of each altitude bin denote the correlation coefficient between the red and black curves.

Fig. 2. RMS (%) differences between lidars and satellite measurements (top). Drifts (% yr^{-1}) calculated from differences between MLS, HALOE and SAGE II datasets. Dashed lines represent the 2σ confidence interval.

correlation coefficients between the two time series are indicated on the right hand side of the figure for each altitude-bin. The time-series are in very good agreement especially in the lower stratosphere at MLO where the mean correlation coefficient is 0.68. At TMF, lower correlations are found (0.38 on average) and almost none at 40 km (0.16). Nevertheless the good agreement elsewhere between the lidar and the merged satellite time-series is further given by the low average bias: $-0.7\,\%$ for MLO and 0.4 for TMF in average.

The errors and drifts between each data set (as a linear trend, Nair et al., 2011) are compared in Fig. 2. On average, the RMS error is lower than 10 % between every instrument for both sites. The highest values (between 10 and 20 %) are found below 24 km. The best agreement is found between MLS and lidar with an RMS error less than 5 %, then follow HALOE and SAGE II with values below 9 %. Except for the values calculated between MLS and lidar at MLO, the altitude variation of the RMS follows the same pattern: minimum at 25 and 35 km, maximum at 30 km and below 25 km. Drifts values are also low, on average below 5 % yr^{-1}. Higher values, close to 5 % yr^{-1}, are found for HALOE in the lower stratosphere (21 km) over MLO and MLS in the upper stratosphere (above 35 km) over TMF. These results support the lack of correlation found at TMF.

Figure 3 shows the lidar ozone anomalies in red and merged satellite time series in black as a function of time. Correlation coefficients were calculated between the two datasets and are written on the right hand side of the figure. Better correlation is obtained at MLO (0.58 on average) and the highest correlation is reached in the ozone maximum
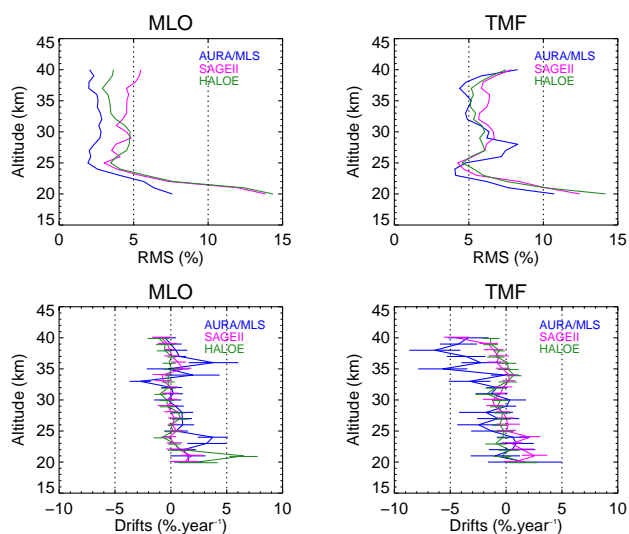
region at 25 km which explains the better agreement in the results than at TMF where ozone anomalies values are much higher.

3 Regression model: description, proxies and specifications

3.1 Model description

To study interannual variations, the ozone mixing ratio monthly means ($O_3(zt)$) were first deseasonalised (i.e., annual and semi-annual components removed by subtracting, for each altitude bin, the composite monthly means computed over the period 1995–2010). To extract each component of interannual variability present in the deseasonalised time series, a zonally asymmetric regression model was applied at each altitude bin (Randel and Cobb, 1994; Ziemke et al., 1997; Li et al., 2008, 2011):

$$O_3(z, t) = \sum_i \alpha_i(z, t) \, \mathrm{proxy}_i(t) + \mathrm{residual}(z, t) \qquad (1)$$

where $\alpha_i(z, t)$ represents the 12, 6, 4 and 3 month seasonal fits of the form: $A_0 + \sum_{i=1}^{7} (\cos i\omega t + \sin i\omega t)$, $\omega = 2\pi \big/ (12\ \text{months})$.

Regression analysis of this type has been widely used in the past (see for example the references in WMO, 2007, chapter 3 and WMO, 2011, chapter 2). A large number of different models and explanatory variables exist. Kerzenmacher et al. (2006) used simulated data to determine criteria for optimised regression analysis. To fulfill these criteria, we chose
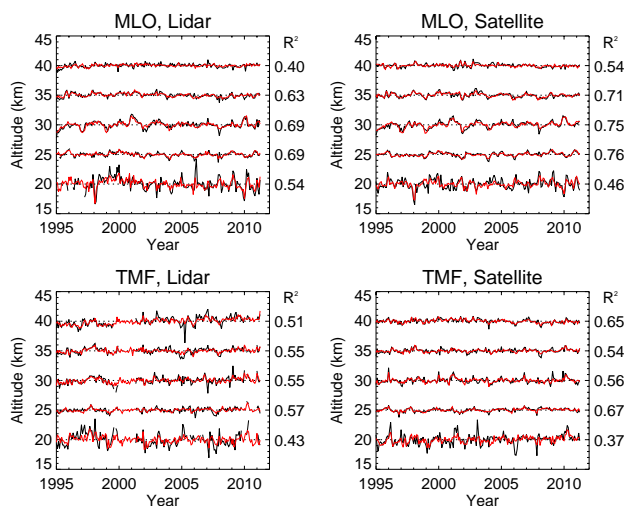
Fig. 3. Time-series of ozone anomalies (black) at 5 km intervals and their corresponding regression fitting results (red) at MLO and TMF for both datasets. The ozone perturbation scale is 10 % km^{-1}. The numbers in front of each dashed line denote the R^2 coefficient given by the fit result.

a time period free of major aerosol loading, i.e., starting in 1995 (four years after the Pinatubo eruption). As the ozone trend is expected to change during our selected time window, we used a nonlinear trend model, which is also advisable when time-series are longer than five years (Kerzenmacher et al., 2006). At TMF, there was a long data gap from April 1999 to May 2001 (see Fig. 1), but the time series extends far enough before and after to allow the detection of the largest changes in ozone trends at mid-latitudes.

3.2 Proxies description

Since our fitting period does not include any major volcanic eruptions, we did not include any aerosol-related proxy in our model. Additionally, for both TMF and MLO we have compared the use of a nonlinear trend and the use of the Ozone Depleting Gas Index (ODGI). A review of all the proxies sources used in our model is shown in Fig. 4. Proxies showing a strong seasonal cycle (Eliassen-Palm flux and transport) were deseasonalised before being used in the model.

The proxy used to represent the 11 yr solar cycle (SC$_{11}$) is the monthly mean of the 10.7 cm^{-1} solar flux measured in Penticton/Ottawa and available at the National Oceanic and Atmospheric Administration (NOAA), at http://www.ngdc.noaa.gov/stp/spaceweather.html).

ENSO signatures in stratospheric ozone and temperature have been observed at low and middle latitudes around the globe and up to fairly high altitudes (Brönnimann et al., 2004; Sassi et al., 2004; Garfinkel and Hartmann, 2007; Li et al., 2008; Hood et al., 2010). To take these effects into account in our model, we chose the bimonthly Multivariate ENSO Index (MEI) values, computed by NOAA

and available at http://www.esrl.noaa.gov/psd/people/klaus.wolter/MEI/.

The Quasi-Biennial Oscillation (QBO) has a strong influence on the interannual variability of ozone (e.g., Baldwin et al., 2001 for a detailed review). Monthly mean values of the zonal wind over Singapore at 50 hPa and at 30 hPa (QBO50 and QBO30) are used. The QBO30 and QBO50 indices are shifted in phase by approximately $\pi/2$. The data were downloaded from the Freien Universität of Berlin website (http://www.geo.fu-berlin.de/en/met/ag/strat/produkte/qbo/), and are updated values from the work of Naujokat (1986). We selected wind anomalies on pressure levels instead of EOF components (Randel and Cobb, 1994) because they yield better coefficients of determination R^2 (simply referred to as R^2 thereafter for brevity) and because our results could be conveniently reported in % per m s^{-1}.

Stratosphere-Troposphere Exchange (STE) and transport of ozone are mainly controlled by the wave driven Brewer-Dobson Circulation (BDC). The strength of the BDC is mainly measured in terms of the Eliassen-Palm flux (EPf). EPf is calculated from the European Centre for Medium Range Weather Forecast (ECMWF) daily operational data following the method of Wohltmann et al. (2007). For TMF, the vertical component of the EPf vector at 100 hPa is averaged spatially over 45–75° N. For MLO, it is averaged over the 3 months preceding the measurement and the first half of the measurement month. The flux through 45–75° S is used for the months from May to October, while the flux through 45–75° N is used for the remaining months.

In addition to EPf, Wohltmann et al. (2005) proposed to separate the processes of horizontal advection and mass convergence (horizontal and vertical transport). After transforming the equivalent latitude profiles, calculated with the daily operational analysis from the ECMWF, into ozone mixing ratio profiles with the help of an ozone climatology, the ozone profiles are integrated using the pressures $p(\lambda, \varphi, t, q)$ computed onto potential temperature levels, thus, incorporating the effect of mass convergence and divergence. Integration is restricted to the isentropic surfaces from 340 to 725 K where transport dominates photochemistry. Then synthetic ozone column obtained in this way could be divided into the two processes of horizontal advection and vertical convergence. Considering a first order development, the mixing ratio and the pressure difference between two isentropic levels are divided in a climatological part mxr$_0$, Δ_0 and an anomaly δmxr, $\delta\Delta$:

$$\sum_i mxr_i \Delta_i = \sum_i (mxr_{0i} + \delta mxr_i)(\Delta_{0i} + \delta\Delta_i) \quad (2)$$

$$= \sum_i mxr_{0i}\Delta_{0i} + \sum_i mxr_{0i}\delta\Delta_i + \sum_i \delta mxr_i \Delta_{0i}$$

$$+ \sum_i \delta mxr_i \delta\Delta_i$$

The first term describes the climatological mean. For our model proxies we used the second term which describes
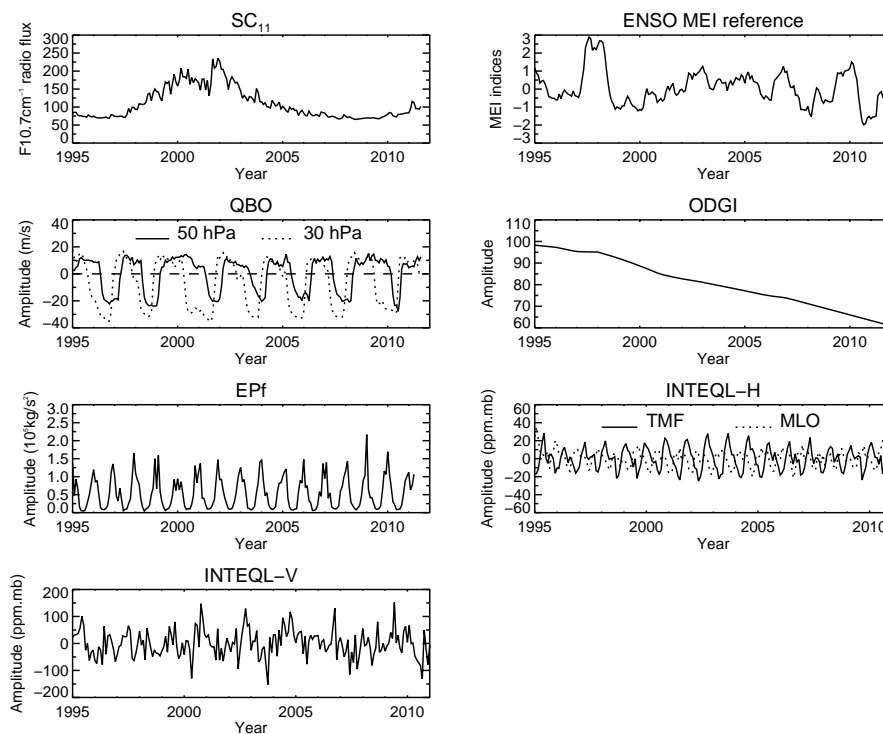
Fig. 4. Proxies used in the model for both stations. For EPf and INTEQL-V, the plots represent the proxy used for TMF.

the vertical changes due to convergence and divergence of mass (INTEQL-V), and the third term, which describes the changes due to horizontal advection (INTEQL-H). The ozone climatology is taken from the National Institute of Water and Atmospheric Research assimilated Total Ozone Mapping Spectrometer and Global Ozone Monitoring Experiment total ozone datasets (Bodeker et al., 2001) available at http://www.iac.ethz.ch/cato/.

Regression models usually use a single or piecewise linear trend to simulate ozone depletion at mid-latitudes due to halogens. As in Brunner et al. (2006), we chose to compare it to a gas index and a direct proxy for the halogen loading of the stratosphere. The effective equivalent stratospheric chlorine (EESC) as defined by the WMO (2007) has commonly been used in the past, instead, we chose to use the Ozone Depleting Gas Index (ODGI) provided by NOAA (http://www.esrl.noaa.gov/gmd/odgi/). ODGI calculation for mid-latitudes is based on EESC values calculated by first taking ground observations of halogen chemicals (estimating the Cl and Br atoms in each chemical), with an additional time lag representing the transport time into the stratosphere (3 yr for mid-latitudes with a 1.5 age spectrum width that also cover the subtropics). The effect of bromine is scaled to take into account its higher ozone destruction efficiency (Newman et al., 2006). Then, defining 100 as the maximum of Equivalent Effective Chlorine (EECL) in the mid-90s and zero in 1980 which corresponds to the values defining full recovery

of the ozone layer in the mid-latitude stratosphere with all other factors remaining constant (Montzka et al., 1996; Hofmann and Montzka, 2009).

In multi-linear analysis, it is assumed that proxies are strictly orthogonal. This condition holds when the determinant of the matrix formed by the decomposed time-series is non-zero. However, to check possible interactions, correlation coefficients were calculated between each proxy for both stations (Table 1 for MLO, Table 2 for TMF). A non-negligible correlation coefficient (-0.5) appears between ENSO and INTEQL-V. The strong correlation between stratosphere/troposphere exchange and ENSO was shown by Zeng and Pyle's simulation (2005). During El Niño and La Niña events, shifts in circulation and meteorological patterns affect the transport of O_3-rich air from the stratosphere to the troposphere. They calculate an anomalously large increase of stratosphere/troposphere exchange following a typical El Niño year. La Niña events result in a decrease of STE. Also, even if the correlation between wind anomalies is not negligible (0.3–0.4), coefficients between ENSO and QBO at 30 hPa, INTEQL-H and QBO at 50 hPa and INTEQL-V and QBO at 50 hPa are smaller than if the first two components of the EOF were used, showing that our choice of proxies is appropriate and that these proxies are mostly orthogonal.

Table 1. Correlation coefficients at MLO between proxies with QBO @ 50 hPa and 30 hPa.

ρ	Solar	ENSO	QBO 50 hPa	QBO 30 hPa	ODGI	EPf	INTEQL-H	INTEQL-V
Solar	1.0	−0.1	0.0	0.0	0.2	0.0	−0.2	0.2
ENSO	−0.1	1.0	0.3	0.0	0.2	0.2	0.0	−0.5
QBO 50 hPa	0.0	0.3	1.0	0.4	0.0	0.0	0.1	0.0
QBO 30 hPa	0.0	0.0	0.4	1.0	0.0	−0.1	0.1	0.1
ODGI	0.2	0.2	0.0	0.0	1.0	−0.1	0.1	−0.1
EPf	0.0	0.2	0.0	−0.1	−0.1	1.0	−0.1	−0.1
INTEQL-H	−0.2	0.0	0.1	0.1	0.1	−0.1	1.0	−0.2
INTEQL-V	0.2	−0.5	0.0	0.1	−0.1	−0.1	−0.2	1.0

Table 2. Correlations coefficients at TMF between proxies with QBO @ 50 hPa and 30 hPa.

ρ	Solar	ENSO	QBO 50 hPa	QBO 30 hPa	ODGI	EPf	INTEQL-H	INTEQL-V
Solar	1.0	−0.1	0.0	0.0	0.2	0.0	0.1	0.0
ENSO	−0.1	1.0	0.3	0.0	0.2	0.1	0.0	0.1
QBO 50 hPa	0.0	0.3	1.0	0.4	0.0	0.0	0.0	0.1
QBO 30 hPa	0.0	0.0	0.4	1.0	0.0	0.0	0.1	0.2
ODGI	0.2	0.2	0.0	0.0	1.0	−0.1	0.0	0.0
EPf	0.0	0.1	0.0	0.0	−0.1	1.0	0.0	0.1
INTEQL-H	0.1	0.0	0.0	0.1	0.0	0.0	1.0	0.0
INTEQL-V	0.0	0.1	0.1	0.2	0.0	0.1	0.0	1.0

3.3 Noise sensitivity and proxy selection

Noise sensitivity of our model was tested by deliberately introducing random noise of varying magnitude in the deseasonalised ozone time series. Values of noise-to-signal ratio of 0.1, 0.5, 1, 2, 5, 10 and 20 were used, and the R^2 values at each altitude bin were computed as a function of this ratio, and plotted in Fig. 5. For both sites, R^2 values reach a minimum when noise values are greater or equal to 5. The convergence towards an asymptotic value shows that the model using atmospheric proxies can mathematically explain variance from the geophysical signal (R^2) with added noise of up to 35 %.

A stepwise backward elimination based on the p-values of the regression coefficients (Mäder et al., 2007) was applied. This method defines a ranked sequence for each proxy at each station. The variable with the lowest rank is dropped from the set of potential explanatory variables. For both stations, the final model includes only the highest ranked variables. Their size is determined by the number of significant variables and the percentage of total explained variance for each proxy (R^2 should be greater than 5 %). The resulting model was fitted twice for each station to take into account the two proxy options selected for trends (ODGI or Linear Trend). The coefficients of determination R^2 were calculated and compared, resulting in a preference for either ODGI or linear trend for each station. While this approach is qualitative in nature, it is robust and avoids the selection of a fixed point in time for the ozone depletion turn-around (WMO,

2007 and 2011) as was required in other studies (Mäder et al., 2010). The proxies and their averaged percentage of total explained variance (in %) are listed in Table 3. This table summarises proxies used in the model for both stations. It results in that the EPf at MLO was not included in the model (R^2 equal 4 %). The R^2 calculated for the linear trend at both stations are also really poor: 1 % at MLO and 3 % at TMF. Noticeably, the use of ODGI instead of a linear trend clearly increases the value of total explained variance for each altitude-bin. The mean difference between the R^2 profiles is ∼ 8 % for MLO and ∼ 9 % for TMF. The largest values are found at 21 km (16 %) for MLO, 26 km (17 %) and between 38 and 44 km (∼ 18 %) for TMF.

3.4 Statistical significance

Statistical significance and seasonal dependences of the main proxies used in the model (SC11, ENSO, ODGI and INTEQL-H) are presented on Fig. 6a and b. The figures show the seasonally dependent responses calculated by the regression analysis for the lidar and satellite time series. The shaded regions indicate that the results are not significant at the 2σ confidence level. The statistical significance is calculated using the T value (derived from the Student's t-in Finlayson, 1987) which equals the ratio of the fitted parameter value to the uncertainty of the fitted parameter. If the T value is greater than 2, the values are considered statistically significant. If not, a gray area is drawn. As the most commonly used proxy, QBO results are significant enough not to be presented here. The EPf proxy is not shown either,

Table 3. Proxies and mean explained variance (noted if over or equal to 5 %) over all altitude bins (lidar values are for each station on the first line and satellite below).

R^2 (%)	Solar	ENSO	QBO (50 and 30)	EPf	INTEQL-H	INTEQL-V	ODGI	LT
MLO	10	14	33	–	8	–	9	–
	10	11	51	–	6		6	–
TMF	13	11	19	8	12	6	19	–
	10	10	27	8	7	5	8	–
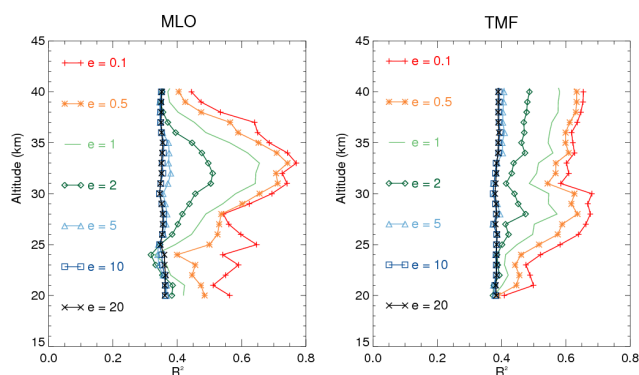
Fig. 5. Coefficient of determination R^2 values given by the noise sensitivity tests realised on the original signal with superimposed noise (see coloured legend for values).

this time due to its low significance, possibly due to the fact that ozone is only transported through mid-latitudes and that vertical transport is restricted to lower and higher latitudes (Wohltmann et al., 2007).

For both stations, similar degrees of significance are observed at the same range of altitude. On exception is for TMF and SC11. In this case, similar positive patterns are observed only between October and December. The lack of measurements at TMF during the solar cycle 23 does not allow us to use lidar results for this proxy. We used the plots of Fig. 6 to select representative altitudes for our subsequent results. At MLO, for SC11, a positive response is observed between 30 and 40 km from spring to fall and opposed to a negative response between 20 and 25 km in winter. ENSO responses are in average positive from spring to fall for both stations in the middle stratosphere and in winter in the upper stratosphere. At MLO, the response in the lower stratosphere is negative early in spring and characterised by a strong negative perturbation. For ODGI, at MLO, a positive response is shown in winter in the middle stratosphere (from January to April at 30 km). Above 30 km, a negative response is shown from September to December. Nevertheless, the strong negative response in the lower stratosphere found with lidar time series is confined to January, May and December on the satellite plot. For horizontal transport, the results obtained from the satellite time series show a higher degree of statistical significance, but the responses are lower in magnitude. At MLO,

two negative similar patterns are observed between 24 and 34 km from January to April. At TMF, a positive response is seen from February to May from 28 to 34 km, followed by a negative one from June to December. The same responses are observed between 20 and 24 km.

For each explanatory variable except EPf (low statistical significance), the lidar and satellite responses will now be detailed and the correlation between these responses will be presented.

4 Results

Figure 3 shows the time-series of the deseasonalised monthly mean ozone anomalies in percent (black curves) between 20 and 40 km. The red superimposed curves are the corresponding reconstructed regression fits. The scale factor is equal to 10 % per km. The regression analysis generally captures well most of the longer timescale variability. The effect of the strong 1997/1998 El Niño (warm ENSO) event is very clear in the lower stratosphere (20 km) in both lidar and satellite ozone anomalies time-series. The total annual mean percentage of variance explained by all components together varies from 40 to 80 %, but generally remains below 60 % (R^2 values in Fig. 3).

4.1 QBO signals

The QBO is the dominant proxy of the model as can be seen on Table 3 where it explains more than 30 % of the total variance at MLO and 19 % at TMF. Figure 7 shows the 2-D contours of the ozone QBO perturbation reconstructed from the two deseasonalised zonal wind time-series used in the regression analysis for the lidars and the satellite time-series at both MLO and TMF locations. The numbers on the right-hand side show the correlation coefficients between the lidars and satellite reconstructed time-series. The clearest QBO signature maximises near 23 and 31 km at MLO and is seasonally synchronised in late winter-early spring and out-of-phase with the equatorial ozone QBO anomaly. An approximate 1 yr phase lag in 2000–2001 is clearly observed, leading to the reversal of the QBO phase before and after 2001, i.e., the positive anomaly (during period of equatorial easterly shear) at 31 km is synchronised to the winter/spring of even years before 2000, and odd years after 2001. High
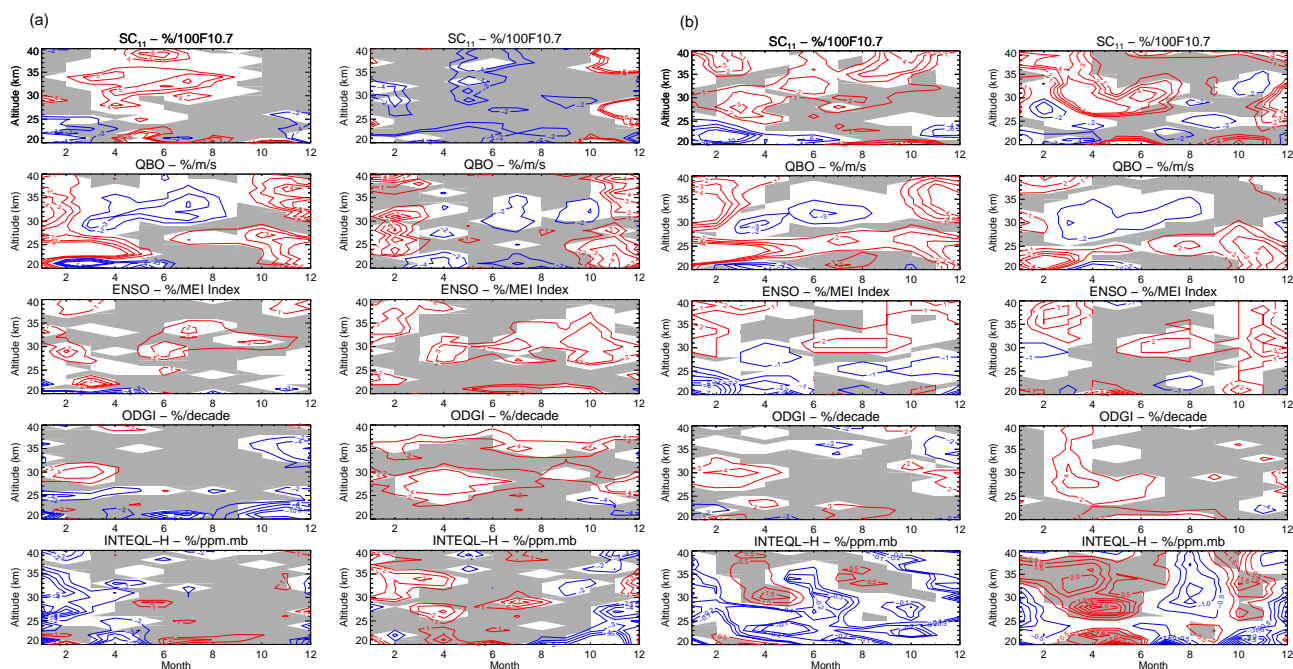
Fig. 6. Seasonally dependent response to the most influent proxies as calculated by the regression analysis with lidar **(a)** and merged satellite **(b)** time series. MLO results are on the left and TMF on the right-hand side. The shaded regions indicate that the results are not significant at the 2σ confidence level, the blue dash contour lines denote the negative values and the red solid contour lines denote positive values.
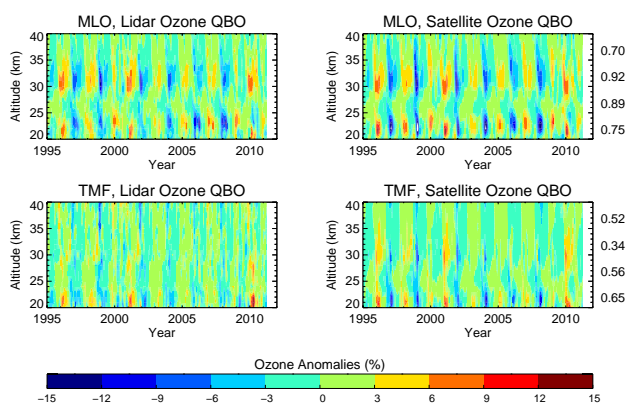

Fig. 7. 2-D contours of the ozone QBO perturbation reconstructed from the regression analysis applied to lidar and satellite data. Correlation coefficients calculated between lidar and satellite responses are indicated on the right-hand side.

correlations found for each altitude between lidar and satellite responses are shown by values greater than 0.7. At TMF (mid-latitude) the QBO signature maximises in January at 31 km and over the entire range (20 to 40 km). The most significant result (at a 2σ level) yields a correlation coefficient of 0.5–0.6 between the lidar and satellite responses between 23 and 36 km. High values (above 0.7 from 20 to 40 km) obtained from interstation cross-correlations (not shown) for lidar and satellite datasets confirm the subtropical regime of MLO.

4.2 11 yr solar cycle signals

Figure 8 (top) shows the reconstructed ozone perturbations, for two different altitudes at MLO (24 and 32 km), illustrating the ozone response to the 11 yr solar cycle (SC_{11}). The response calculated from the lidar and satellite time-series is plotted using solid and dotted lines, respectively. The correlation coefficients were found to maximise at 24 (0.7) and 32 km (0.9). The lower stratosphere response (below 30 km) is characterised by a strong negative response observed during the 1999–2002 solar maximum, and a positive response is observed during the 2006–2009 solar minimum. A stronger response is seen in the satellite time-series. The lidar response is narrower and maximises in January. This response computed from the lidar and satellite time-series is also produced in the model simulations of Austin et al. (2007) where it is partially explained by the QBO and by a change in the upwelling due to SST variations. Theoretical and observational evidence favours relative downwelling in the tropics near solar maxima (Kodera and Kuroda, 2002; Hood and Soukharev, 2003). According to these simulations, and to the analysis presented by Marsh and Garcia (2007), variability in lower-stratospheric ozone is strongly related to changes in tropical upwelling associated with ENSO. At 33 km, a weak expected positive response (3 to 6 %) is observed in spring on the lidar reconstructed response during the solar maximum (cycle 23 maximum, from 2000 to 2002), but only during the 2002 winter on the satellite reconstructed response
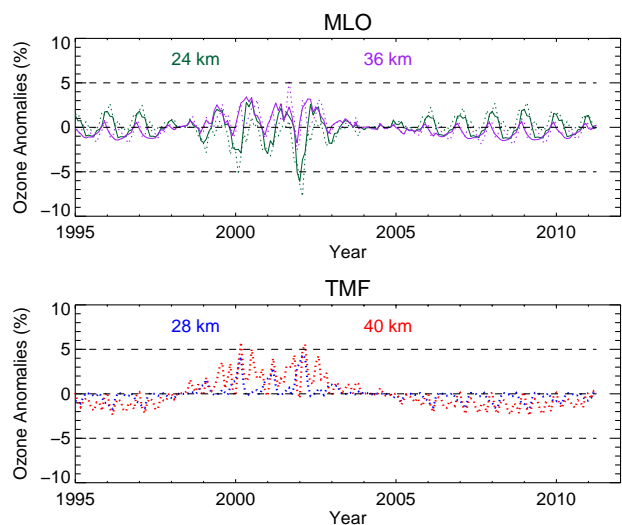
Fig. 8. Ozone response to SC_{11} perturbations at different altitude over MLO and TMF. Lidar responses are solid lines and satellite are dotted lines.

Fig. 9. Ozone response to ENSO perturbations at 22 (blue) and 30 (red) km over MLO and TMF. Lidar responses are solid lines and satellite are dotted lines.

(Soukharev et Hood, 2006). Further investigation is needed to fully understand and interpret these features.

Figure 8 (bottom) shows the reconstructed ozone perturbations at TMF at 28 and 40 km (satellite dataset only). No result is shown for the lidar dataset due to the lack of measurements during the solar cycle 23 maximum. The satellite responses shown at 28 and 40 km on the right hand side of Fig. 8 expose a clear winter positive response during the solar maxima. This winter response expend until spring as the altitude increase. Then this response become negative during solar minima.

4.3 ENSO signals

The highest correlation coefficients (more than 0.6) between the lidar and satellite responses were found between 25 and 35 km at MLO and above 30 km at TMF. Figure 9 shows responses at 26 and 34 km over both stations. The response to the strong El Niño event in 1997/98 is clear at both sites in both the lidar and satellite time-series. Positive ozone anomalies were found above 30 km over MLO as well as over TMF for the whole altitude range. A negative signature, out-of-phase with the one above, is observed at MLO in the lower stratosphere. The response to the strong 2010 Niña event is out-of-phase with the 1997 response to El Niño. These signatures were observed in the different CCM's simulations made by Fisher et al. (2008) and Cagnazzo et al. (2009). Using satellite datasets and GCM simulations, Hood et al. (2010) showed that the negative response and weaker cooling (see trends above MLO in Li et al., 2011) observed throughout the tropical lower stratosphere are attributable to an indirect dynamical effect, i.e., an acceleration of the Brewer-Dobson circulation as a result of enhanced Rossby wave activity as-
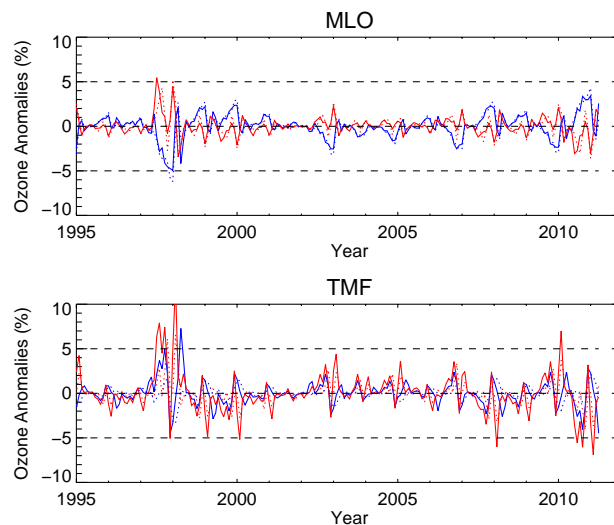
sociated with the tropical tropospheric circulation changes. However, at MLO, the lidar and satellite responses show some discrepancies, especially in the lower stratosphere. Until the Niña event in 2010, both responses are synchronised in January and appear if the MEI index value is above 1 for an El Niño event and −1 for a Niña. The lidar response is an early winter positive response to a Niña event followed by a negative response at the end of the winter.

4.4 Trends and response to the ODGI

Seeking trends in time-series is usually done with a piecewise or single linear trend or with an EESC representation (WMO, 2010). As previously mentioned, the ODGI was preferred as a new index based on EESC calculations. Figure 10 (left) shows the total explained variance calculated with ODGI minus the total explained variance calculated with a linear trend component. It clearly appears that the use of ODGI increases the value of total explained variance at each altitude-bin, particularly at TMF. The mean difference between the profiles is ∼ 5 % for MLO and ∼ 9 % for TMF. The highest values of explained variance are obtained at 22 km (18 %) for MLO, at 28 km (18 %) and at 40 km (∼ 20 %) for TMF. The centre and right panels of Fig. 9 show the correlation coefficients between the linear trend and the ODGI responses. At all altitude over MLO and mainly at TMF, values of this coefficient are around 0.5. At TMF, two peaks of higher values can be seen at 28 (0.6) and 40 km (0.9). A major difference between the ODGI and linear response is found before the transition period (see definition below). The structure of the ODGI allows the model to take into account the state of the atmosphere before 1995 when the classic linear trend define the first year of the analysis as a start of the potential recovery.
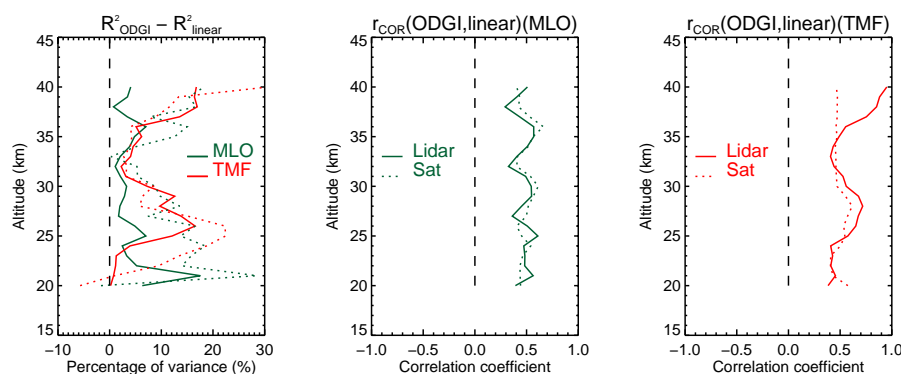
Fig. 10. Left: the difference between the total explained variance calculated with the ODGI or a linear trend with lidar (solid line) and satellite (dotted line) time series. The red colour is use to represent TMF and the green MLO. Centre: correlation coefficient calculated between ozone ODGI and ozone linear response at MLO for both datasets. Right: same for TMF.

Figure 11 shows the 2-D contours of the ozone ODGI perturbations reconstructed from the regression analysis. The peak-to-peak annual mean values (compared to linear trends) over the entire time period are compiled in Table 4.

A good correlation is found at MLO between the lidar and satellite time-series especially in the middle and lower stratosphere. Four layers of distinct signatures appear: a layer of strong ozone decrease in the lower stratosphere (20–22 km) in phase with a layer of weak decrease at 36 km, and two layers of slow ozone increase at 30 and 42 km. The upper stratospheric increase and the steady lower stratospheric decrease agree well with the multi-model simulations made by Eyring et al. (2010). The upper stratospheric signature is a direct response to the decrease of total atmospheric chlorine resulting from the Montreal Protocol, though the role of the CO_2-induced stratospheric cooling still need to be investigated (Randel et al., 2009; Li et al., 2011). The lower stratospheric signature is attributed to a faster transit of air through the tropical lower stratosphere from enhanced tropical upwelling, leading to less time for ozone production, hence to lower ozone levels in this region (Randel and Thompson, 2011).

At TMF, the best agreement between the lidar and satellite datasets is found near 28 km. The steady increase starting in 2004 contrasts with MLO's tropical case. The temperature evolution in the mid-latitude lower stratosphere is similar to that in the tropics, though the temperature response is more sensitive to changes in ODSs through ODS induced change (WMO, 2007; Shepherd and Jonsson, 2008). The largest peak-to-peak values obtained from the lidar time-series are found in the photochemically controlled upper stratosphere (44 km), and can be partially explained by the cooling of the stratosphere (Li et al., 2011) slowing down chemical destruction rates, thus, increasing ozone. However, caution must be used in this interpretation due to the lack of quantitative agreement at this altitude between the lidar and satellite results. Due to the very low ozone number density above
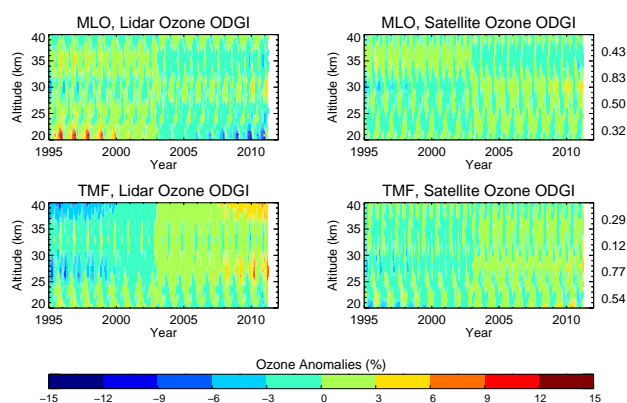

Fig. 11. 2-D contours of the ozone ODGI response reconstructed from the regression analysis applied to lidar and satellite data. Correlation coefficients calculated between lidar and satellite responses are indicated on the right-hand side.

40 km, the lidar measurement loses sensitivity and is, therefore, affected by lower signal-to-noise ratios.

To better identify the ozone trend turning point and its shift in time with latitude, the annual mean (in percent by decade) of the ODGI responses were calculated and compiled in Table 4. The transition period is identified as the shift between negative and positive values at ± 1 %. Over TMF, at 28 km, the time transition was established between 2000 and 2006 and between 2001 and 2004 at 40 km. The start of the change in ozone recovery (~ 2000) corresponds to the shift found by Waugh et al. (2009) over the Northern Hemisphere midlatitudes.

One striking difference between the lidar and satellite reconstructed responses is the significantly larger amplitudes computed from the lidar time series. Differences in the vertical resolution and in the remote-sensing methods, as well as the quality of the spatial and temporal coincidences are the most probable causes of these differences (Li et al., 2008; Randel et al., 2009).

Table 4. Summary of the extreme annual mean values of the ozone response to the ODGI (lidar values are for each altitude on the first line, satellite below and linear on the right). Results calculated from the lidar stratospheric ozone column from 20 to 40 km were added on the bottom of the table. Units are in % by decade.

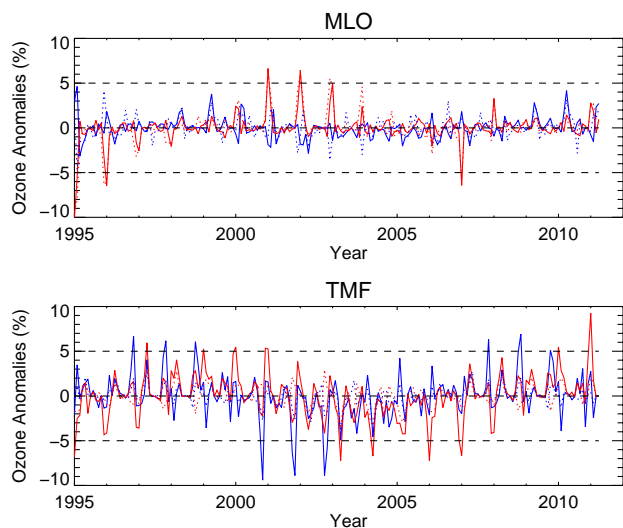|	MLO			TMF	
20 km	-8.1 ± 0.5	-1.0 ± 0.1	28 km	4.9 ± 0.2	0.8 ± 0.1
	0.0 ± 0.1	0.1 ± 0.1		2.4 ± 1.5	0.4 ± 0.0
36 km	-1.9 ± 1.1	-0.3 ± 0.0	40 km	12.3 ± 0.3	2.2 ± 0.1
	-1.7 ± 0.1	-0.3 ± 0.0		-2.9 ± 0.1	-0.5 ± 0.0
Column	-1.5 ± 0.2	-0.3 ± 0.1	Column	2.1 ± 0.3	0.4 ± 0.1

Fig. 12. Ozone response to INTEQL-H perturbations at 22 (blue) and 34 (red) km over MLO and TMF. Lidar responses are solid lines and satellite are dotted lines.

4.5 Horizontal and vertical transport

Figure 12 presents ozone responses to INTEQL-H (horizontal transport proxy) at 22 and 34 km, altitudes below the stratospheric ozone mixing ratio maximum which marks the end of the region of dynamical influence. Good agreement is found between the responses for the lidar and satellite time-series. Over both sites, an early winter signature was identified. Some correlation with the 11 yr solar cycle can also be seen. At MLO, at 34 km and generally the middle stratosphere, the response is characterised by a positive signature in-phase with the solar cycle 23 maximum, in good agreement with the satellite response. Below, the response to the cycle 23 maximum is positive with the lidar dataset and negative with the satellite dataset. The response at TMF is characterised by a negative signature out-of-phase with the solar cycle 23 maximum at 22 km. Above, the response is also out-of-phase but starts two years later.

Table 1 shows the correlation coefficients between the proxies used in the model over MLO. The correlation between ENSO and INTEQL-V, equal to -0.5, is too high

to consider these two components orthogonal. Connection between these two proxies is not surprising considering the strong connection between ENSO events and the vertical component of the mean upper tropospheric and lower-stratospheric circulation. The suppressed convection in the western Pacific leads to less efficient vertical transport of low concentrations of ozone from the surface. In contrast, a negative ozone anomaly in the eastern Pacific arises from increased humidity and enhanced upward transport (Doherty et al., 2006; Chandra et al., 2007). Moreover, during El Niño and La Niña events, shifts in circulation and meteorological patterns not only affect photochemistry in the tropics, but also the transport of ozone-rich air from the stratosphere to the troposphere (Zeng and Pyle, 2005). Note also that in the tropics during ENSO, warmer sea surface temperatures lead to a warmer troposphere and a higher tropopause throughout most of the tropics. Higher tropopause levels are associated with lower tropical ozone and increased ascent in the lower stratosphere circulation, thus, increasing the Brewer-Dobson circulation (Cagnazzo et al., 2009). Over TMF, no significant signatures were identified.

5 Summary and conclusion

This study presented a multi-linear regression analysis using ~ 17 yr of stratospheric ozone measurements by lidar and satellite-borne instruments above Table Mountain, California and Mauna Loa, Hawaii (20 to 40 km). Comparisons between the lidar and satellite data sets generally showed good agreement and revealed only low biases and drift values.

As the dominant feature, the ozone QBO explained the largest fraction of the total variance (up to 60 %) with an amplitude of 5 % throughout the stratosphere. The QBO response is characterised by a winter signature which is different for the two stations: at MLO, the lower stratosphere signature is in-phase with that in the middle stratosphere and out-of-phase with that in the upper stratosphere whereas at TMF the lower middle, and upper stratosphere signatures are in-phase.

Several 11 yr solar cycle and ENSO signatures were clearly identified at MLO for the lidar and satellite datasets, both showing a negative response in the lower stratosphere

(-5 to -2 %/100 F.7 and MEI index). This response has been attributed by modellers to a change in tropical upwelling subsequently strengthening the Brewer-Dobson circulation.

Our regression analysis model was used to extract the stratospheric ozone response to the decrease of ozone-depleting substances (ODGI) and compare it to the more classical linear trend. Choosing an ODGI-based proxy over a linear trend significantly increased the total variance explained by the model fits (overall mean ~ 10 %). The ozone response to the decrease of ODGI is significantly negative in the lower stratosphere above MLO which is a symptom of an increase of the Brewer-Dobson circulation. At TMF, significant positive trends are found in the upper stratosphere and the positive response to the Montreal protocol can finally be seen on the lidar time series.

The inclusion in the regression model of two indices representing horizontal and vertical transport was tested. At MLO, the vertical transport index is highly correlated with the ENSO (MEI) index (expected from model results). No significant response could be associated with this index. However, a statistically significant ozone response to the horizontal transport index was found between 20 and 35 km for both the lidar and satellite datasets. Over MLO, the seasonal response is enhanced and becomes positive during the solar maximum. At TMF, an early (late) positive (negative) response is observed when the cycle 23 is rising (setting).

This study covered 17 consecutive years without heavy aerosol loading in the stratosphere, but only includes one and a half solar cycles. The consistency found with model simulations is very encouraging and points towards promising results once a full second solar cycle (and beyond) is covered. Hence, the study shows the need for high quality continued, long-term, routine measurements by the JPL lidars at TMF and MLO, as well as other ground-based instruments and satellite missions.

Edited by: S. Godin-Beekmann

References

Austin, J., Hood, L. L., and Soukharev, B. E.: Solar cycle variations of stratospheric ozone and temperature in simulations of a coupled chemistry-climate model, Atmos. Chem. Phys., 7, 1693–1706, doi:10.5194/acp-7-1693-2007, 2007.

Baldwin, M. P., Gray, L. J., Dunkerton, T. J., Hamilton, K., Haynes, P. H., Randel, W. J., Holton, J. R., Alexander, M. J., Hirota, I., Horinouchi, T., Jones, D. B. A., Kinnersley, J. S., Marquardt, C., Sato, K., and Takahashi, M.: The quasi-biennial oscillation, Rev. Geophys., 39, 179–229, doi:10.1029/1999RG000073, 2001.

Bhatt, P. P., Remsberg, E. E., Gordley, L. L., McInerney, M. J., Brackett, V. G., and Russell III, J. M.: An evaluation of the quality of Halogen Occultation Experiment ozone profiles in the lower stratosphere, J. Geophys. Res., 104, 9261–9275, 1999.

Bodeker, G. E., Scott, J. C., Kreher, K., and McKenzie, R. L.: Global ozone trends in potential vorticity coordinates using TOMS and GOME intercompared against the Dobson network: 1978–1998, J. Geophys. Res., 106, 23029–23042, doi:10.1029/2001JD900220, 2001.

Brönnimann S., Luterbacher, J., Staehelin, J., Svendby, T. M., Hansen, G., and Svenøe, T.: Extreme Climate of the Global Tropopsphere and Stratosphere 1940–1942 related to El Nino, Nature, 431, 971–974, 2004.

Brunner, D., Staehelin, J., Künsch, H.-R., and Bodeker, G. E.: A Kalman filter reconstruction of the vertical ozone distribution in an equivalent latitude–potential temperature framework from TOMS/GOME/SBUV total ozone observations, J. Geophys. Res., 111, D12308, doi:10.1029/2005JD006279, 2006.

Cagnazzo, C., Manzini, E., Calvo, N., Douglass, A., Akiyoshi, H., Bekki, S., Chipperfield, M., Dameris, M., Deushi, M., Fischer, A. M., Garny, H., Gettelman, A., Giorgetta, M. A., Plummer, D., Rozanov, E., Shepherd, T. G., Shibata, K., Stenke, A., Struthers, H., and Tian, W.: Northern winter stratospheric temperature and ozone responses to ENSO inferred from an ensemble of Chemistry Climate Models, Atmos. Chem. Phys., 9, 8935–8948, doi:10.5194/acp-9-8935-2009, 2009.

Chandra, S., Ziemke, J. R., Schoeberl, M. R., Froidevaux, L., Read, W. G., Levelt, P. F., and Bhartia, P. K.: Effects of the 2004 El Niño on tropospheric ozone and water vapor, Geophys. Res. Lett., 34, L06802, doi:10.1029/2006GL028779, 2007.

Dhomse, S., Weber, M., Wohltmann, I., Rex, M., and Burrows, J. P.: On the possible causes of recent increases in northern hemispheric total ozone from a statistical analysis of satellite data from 1979 to 2003, Atmos. Chem. Phys., 6, 1165–1180, doi:10.5194/acp-6-1165-2006, 2006.

Doherty, R. M., Stevenson, D. S., Johnson, C. E., Collins, W. J., and Sanderson, M. G.: Tropospheric ozone and El Niño–Southern Oscillation: Influence of atmospheric dynamics, biomass burning emissions, and future climate change, J. Geophys. Res., 111, D19304, doi:10.1029/2005JD006849, 2006.

Eyring, V., Cionni, I., Bodeker, G. E., Charlton-Perez, A. J., Kinnison, D. E., Scinocca, J. F., Waugh, D. W., Akiyoshi, H., Bekki, S., Chipperfield, M. P., Dameris, M., Dhomse, S., Frith, S. M., Garny, H., Gettelman, A., Kubin, A., Langematz, U., Mancini, E., Marchand, M., Nakamura, T., Oman, L. D., Pawson, S., Pitari, G., Plummer, D. A., Rozanov, E., Shepherd, T. G., Shibata, K., Tian, W., Braesicke, P., Hardiman, S. C., Lamarque, J. F., Morgenstern, O., Pyle, J. A., Smale, D., and Yamashita, Y.: Multi-model assessment of stratospheric ozone return dates and ozone

recovery in CCMVal-2 models, Atmos. Chem. Phys., 10, 9451–9472, doi:10.5194/acp-10-9451-2010, 2010.

Finlayson, B. A.: Numerical recipes: The art of scientific computing, edited by: Press, W. H., Flanner, B. P., Teukolsky, S. A., and Vetterling, W. T., Cambridge University Press, 1986, 818 pp., 1987.

Fischer, A. M., Shindell, D. T., Winter, B., Bourqui, M. S., Faluvegi, G., Rozanov, E., Schraner, M., and Brönnimann, S.: Stratospheric winter climate response to ENSO in three chemistry-climate models, Geophys. Res. Lett., 35, L13819, doi:10.1029/2008GL034289, 2008.

Froidevaux, L., Jiang, Y. B., Lambert, A., Livesey, N. J., Read, W. G., Waters, J. W., Browell, E. V., Hair, J. W., Avery, M. A., McGee, T. J., Twigg, L. W., Sumnicht, G. K., Jucks, K. W., Margitan, J. J., Sen, B., Stachnik, R. A., Toon, G. C., Bernath, P. F., Boone, C. D., Walker, K. A., Filipiak, M. J., Harwood, R. S., Fuller, R. A., Manney, G. L., Schwartz, M. J., Daffer, W. H., Drouin, B. J., Cofield, R. E., Cuddy, D. T., Jarnot, R. F., Knosp, B. W., Perun, V. S., Snyder, W. V., Stek, P. C., Thurstans, R. P., and Wagner, P. A.: Validation of Aura Microwave Limb Sounder stratospheric ozone measurements, J. Geophys. Res., 113, D15S20, doi:10.1029/2007JD008771, 2008.

Garfinkel, C. I. and Hartmann, D. L.: Effects of the El Niño–Southern Oscillation and the Quasi-Biennial Oscillation on polar temperatures in the stratosphere, J. Geophys. Res., 112, D19112, doi:10.1029/2007JD008481, 2007.

Hofmann, D. J. and Montzka, S. A.: Recovery of the Ozone Layer: The Ozone Depleting Gas Index, Eos Trans. AGU, 90, 1, doi:10.1029/2009EO010001, 2009.

Hood, L. L. and Soukharev, B. E.: Quasi-Decadal Variability of the Tropical Lower Stratosphere: The Role of Extratropical Wave Forcing, J. Atmos. Sci., 60, 2389–2403, 2003.

Hood, L. L., Soukharev, B. E., and McCormack, J. P.: Decadal variability of the tropical stratosphere: Secondary influence of the El Niño–Southern Oscillation, J. Geophys. Res., 115, D11113, doi:10.1029/2009JD012291, 2010.

Jain, M.: Trend in stratospheric ozone over tropics, J. Geophys. Res., 115, D19311, doi:10.1029/2009JD012612, 2010.

Jones, A., Urban, J., Murtagh, D. P., Eriksson, P., Brohede, S., Haley, C., Degenstein, D., Bourassa, A., von Savigny, C., Sonkaew, T., Rozanov, A., Bovensmann, H., and Burrows, J.: Evolution of stratospheric ozone and water vapour time series studied with satellite measurements, Atmos. Chem. Phys., 9, 6055–6075, doi:10.5194/acp-9-6055-2009, 2009.

Jrrar, A., Braesicke, P., Hadjinicolaou, P., and Pyle, J. A.: Trend analysis of CTM-derived northern hemisphere winter total ozone using self-consistent proxies: How well can we explain dynamically induced trends?, Q. J. Roy. Meteorol. Soc., 132, 1969–1983, doi:10.1256/qj.05.136, 2006.

Kerzenmacher, T., Keckhut, P., Hauchecorne, A., and Chanin, M.: Methodological uncertainties in multi-regression analyses of middle atmospheric data series, J. Environ. Monit., 8, 682–690, doi:10.1039/b603750j, 2006.

Kodera, K. and Kuroda, Y.: Dynamical response to the solar cycle, J. Geophys. Res., 107, 4749, doi:10.1029/2002JD002224, 2002.

Leblanc, T. and McDermid, I. S.: Stratospheric ozone climatology from lidar measurements at Table Mountain (34.4° N, 117.7° W) and Mauna Loa (19.5° N, 155.6° W), J. Geophys. Res., 105, 14613–14623, doi:10.1029/2000JD900030, 2000.

Leblanc, T. and McDermid, I. S.: Quasi-biennial oscillation signatures in ozone and temperature observed by lidar at Mauna Loa, Hawaii (19.5° N, 155.6° W), J. Geophys. Res., 106, 14869–14874, doi:10.1029/2001JD900162, 2001.

Leblanc, T., Tripathi, O. P., McDermid, I. S., Froidevaux, L., Livesey, N. J., Read, W. G., and Waters, J. W.: Simultaneous lidar and EOS MLS measurements, and modeling, of a rare polar ozone filament event over Mauna Loa Observatory, Hawaii, Geophys. Res. Lett., 33, L16801, doi:10.1029/2006gl026257, 2006.

Li, F., Stolarski, R. S., and Newman, P. A.: Stratospheric ozone in the post-CFC era, Atmos. Chem. Phys., 9, 2207–2213, doi:10.5194/acp-9-2207-2009, 2009.

Li, T., Leblanc, T., and McDermid, I. S.: Interannual variations of middle atmospheric temperature as measured by the JPL lidar at Mauna Loa Observatory, Hawaii (19.5N, 155.6W), J. Geophys. Res., 113, D14109, doi:10.1029/2007JD009764, 2008.

Li, T., Leblanc, T., McDermid, I. S., Keckhut, P., Hauchecorne, A., and Dou, X.: Middle atmosphere temperature trend and solar cycle revealed by long-term Rayleigh lidar observations, J. Geophys. Res., 116, D00P05, doi:10.1029/2010JD015275, 2011.

Mäder, J. A., Staehelin, J., Brunner, D., Stahel, W. A., Wohltmann, I., and Peter, T.: Statistical modeling of total ozone: Selection of appropriate explanatory variables, J. Geophys. Res., 112, D11108, doi:10.1029/2006JD007694, 2007.

Mäder, J. A., Staehelin, J., Peter, T., Brunner, D., Rieder, H. E., and Stahel, W. A.: Evidence for the effectiveness of the Montreal Protocol to protect the ozone layer, Atmos. Chem. Phys., 10, 12161–12171, doi:10.5194/acp-10-12161-2010, 2010.

Manney, G. L., Michelsen, H. A., Bevilacqua, R. M., Gunson M. R., Irion, F. W., Livesey, N. J., Oberheide, J., Riese, M., Russell III, J. M., Toon, G. C., and Zawodny, J. M.: Comparison of satellite ozone observations in coincident air masses in early November 1994, J. Geophys. Res., 106, 9923–9943, 2001.

Marsh, D. R. and Garcia, R. R.: Attribution of decadal variability in lower-stratospheric tropical ozone, Geophys. Res. Lett., 34, L21807, doi:10.1029/2007GL030935, 2007.

McConnell, J. C. and Jin, J. J.: Stratospheric ozone chemistry, Atmosphere-Ocean, 46, 69–92, 2008.

Montzka, S. A., Butler, J. H., Myers, R. C., Thompson, T. M., Swanson, T. H., Clarke, A. D., Lock, L. T., and Elkins, J. W.: Decline in the tropospheric abundance of halogen from halocarbons: Implications for stratospheric ozone depletion, Science, 272, 1318–1322, 1996.

Naujokat, B.: An update of the observed quasi-biennial oscillation of the stratospheric winds over the tropics, J. Atmos. Sci., 43, 1873–1877, 1986.

Nair, P. J., Godin-Beekmann, S., Pazmiño, A., Hauchecorne, A., Ancellet, G., Petropavlovskikh, I., Flynn, L. E., and Froidevaux, L.: Coherence of long-term stratospheric ozone vertical distribution time series used for the study of ozone recovery at a northern mid-latitude station, Atmos. Chem. Phys., 11, 4957–4975, doi:10.5194/acp-11-4957-2011, 2011.

Newman, P. A., Nash, E. R., Kawa, S. R., Montzka, S. A., and Schauffler, S. M.: When will the Antarctic ozone hole recover? Geophys. Res. Lett., 33, L12814, doi:10.1029/2005GL025232, 2006.

Randel, W. J. and Cobb, J. B.: Coherent variations of monthly mean total ozone and lower stratospheric temperature, J. Geophys. Res., 99, 5433–5447, doi:10.1029/93JD03454, 1994.

Randel, W. J. and Thompson, A. M.:Interannual variability and trends in tropical ozone derived from SAGE II satellite data and SHADOZ ozonesondes, J. Geophys. Res., 116, D07303, doi:10.1029/2010JD015195, 2011.

Randel, W. J., Shine, K. P., Austin, J., Barnett, J., Claud, C., Gillett, N. P., Keckhut, P., Langematz, U., Lin, R., Long, C., Mears, C., Miller, A., Nash, J., Seidel, D. J., Thompson, D. W. J., Wu, F., and Yoden, S.: An update of observed stratospheric temperature trends, J. Geophys. Res., 114, D02107, doi:10.1029/2008JD010421, 2009.

Reinsel, G. C., Miller, A. J., Weatherhead, E. C., Flynn, L. E., Nagatani, R. M., Tiao, G. C., and Wuebbles, D. J.: Trend analysis of total ozone data for turnaround and dynamical contributions, J. Geophys. Res., 110, D16306, doi:10.1029/2004JD004662, 2005.

Remsberg, E. E.: On the response of Halogen Occultation Experiment (HALOE) stratospheric ozone and temperature to the 11-year solar cycle forcing, J. Geophys. Res., 113, D22304, doi:10.1029/2008JD010189, 2008.

Sassi, F., Kinnison, D., Boville, B. A., Garcia, R. R., and Roble, R.: Effect of El Niño–Southern Oscillation on the dynamical, thermal, and chemical structure of the middle atmosphere, J. Geophys. Res., 109, D17108, doi:10.1029/2003JD004434, 2004.

Shepherd, T. G.: Dynamics, stratospheric ozone, and climate change, Atmos.-Ocean, 46, 117–138, 2008.

Shepherd, T. G. and Jonsson, A. I.: On the attribution of stratospheric ozone and temperature changes to changes in ozone-depleting substances and well-mixed greenhouse gases, Atmos. Chem. Phys., 8, 1435–1444, doi:10.5194/acp-8-1435-2008, 2008.

Soukharev, B. E. and Hood, L. L.: Solar cycle variation of stratospheric ozone: Multiple regression analysis of long-term satellite data sets and comparisons with models, J. Geophys. Res., 111, D20314, doi:10.1029/2006JD007107, 2006.

Steinbrecht, W., Claude, H., Schoenenborn, F., McDermid, I. S., LeBlanc, T., Godin-Beekmann, S., Keckhut, P., Hauchecorne, A., Van Gijsel, J. A. E., Swart, D. P. J., Bodeker, G., Parrish, A., Boyd, I., Kämpfer, N., Hocke, K., Stolarski, R. S., Frith, S. M., Thomason, L. W., Remsberg, E. E., Von Savigny, C., Rozanov, A., and Burrows, J. B.: Ozone and temperature trends in the upper stratosphere at five stations of the Network for the Detection of Atmospheric Composition Change, Int. J. Remote Sens., 30, 3875–3886, doi:10.1080/01431160902821841, 2009.

Tatarov, B., Nakane, H., Park, Ch. B., Sugimoto, N., and Matsui, I.: Lidar observation of long-term trends and variations of stratospheric ozone and temperature over Tsukuba, Japan, Int. J. Remote Sens., 30, 3951–3960, doi:10.1080/01431160902821882, 2009.

Waugh, D. W., Oman, L., Kawa, S. R., Stolarski, R. S., Pawson, S., Douglass, A. R., Newman, P. A., and Nielsen, J. E.: Impacts of climate change on stratospheric ozone recovery, Geophys. Res. Lett., 36, L03805, doi:10.1029/2008GL036223, 2009.

WMO (World Meteorological Organization): Scientific Assessment of Ozone Depletion: 1998, Global Ozone Research and Monitoring Project – Report No. 44, Geneva, Switzerland, 1999.

WMO (World Meteorological Organization): Scientific Assessment of Ozone Depletion: 2006, Global Ozone Research and Monitoring Project – Report No. 50, 572 pp., Geneva, Switzerland, 2007.

WMO (World Meteorological Organization): Scientific Assessment of Ozone Depletion: 2010, Global Ozone Research and Monitoring Project – Report No. 52, 516 pp., Geneva, Switzerland, 2011.

Wohltmann, I., Rex, M., Brunner, D., and Mäder, J.: Integrated equivalent latitude as a proxy for dynamical changes in ozone column, Geophys. Res. Lett., 32, L09811, doi:10.1029/2005GL022497, 2005.

Wohltmann, I., Lehmann, R., Rex, M., Brunner, D., and Mäder, J. A.: A process-oriented regression model for column ozone, J. Geophys. Res., 112, D12304, doi:10.1029/2006JD007573, 2007.

Zeng, G. and Pyle, J. A.: Influence of El Niño Southern Oscillation on stratosphere/troposphere exchange and the global tropospheric ozone budget, Geophys. Res. Lett., 32, L01814, doi:10.1029/2004GL021353, 2005.

Ziemke, J., Chandra, S., McPeters, R., and Newman, P.: Dynamical proxies of column ozone with applications to global trend models, J. Geophys. Res., 102, 6117–6129, 1997.